remote sensing

MDPI

Article

Integrating SBAS-InSAR and AT-LSTM for Time-Series Analysis and Prediction Method of Ground Subsidence in Mining Areas

Yahong Liu and Jin Zhang *

College of Mining Engineering, Taiyuan University of Technology, Taiyuan 030024, China; liuyahong0103@link.tyut.edu.cn

* Correspondence: zhangjin@tyut.edu.cn

Abstract: Ground subsidence is a significant safety concern in mining regions, making large-scale subsidence forecasting vital for mine site environmental management. This study proposes a deep learning-based prediction approach to address the challenges posed by the existing prediction methods, such as complicated model parameters or large data requirements. Small baseline subset interferometric synthetic aperture radar (SBAS-InSAR) technology was utilized to collect spatiotemporal ground subsidence data at the Pingshuo mining area from 2019 to 2022, which was then analyzed using the long-short term memory (LSTM) neural network algorithm. Additionally, an attention mechanism was introduced to incorporate temporal dependencies and improve prediction accuracy, leading to the development of the AT-LSTM model. The results demonstrate that the Pingshuo mine area had subsidence rates ranging from −205.89 to −59.70 mm/yr from 2019 to 2022, with subsidence areas mainly located around Jinggong-1 (JG-1) and the three open-pit mines, strongly linked to mining activities, and the subsidence range continuously expanding. The spatial distribution of the AT-LSTM prediction results is basically consistent with the real situation, and the correlation coefficient is more than 0.97. Compared with the LSTM, the AT-LSTM method better captured the fluctuation changes of the time series for fitting, while the model was more sensitive to the mining method of the mine, and had different expressiveness in open-pit and shaft mines. Furthermore, in comparison to existing time-series forecasting methods, the AT-LSTM is effective and practical.

Keywords: mining area; ground subsidence; small baseline subset interferometric synthetic aperture radar (SBAS-InSAR); long short-term memory (LSTM); attention mechanism

Citation: Liu, Y.; Zhang, J. Integrating SBAS-InSAR and AT-LSTM for Time-Series Analysis and Prediction Method of Ground Subsidence in Mining Areas. *Remote Sens.* **2023**, *15*, 3409. https://doi.org/10.3390/rs15133409

Academic Editor: Paraskevas Tsangaratos

Received: 18 April 2023
Revised: 13 June 2023
Accepted: 2 July 2023
Published: 5 July 2023

1. Introduction

Coal resources are a vital component of the energy industry, serving as a critical material basis for the sustainable development of human society [1,2]. As a major producer and user of coal resources, China has a long history of mining, which has made a significant contribution to the country's economy [3,4]. However, continued mining activities have been shown to have negative environmental impacts [5], with the geological hazards it causes being a key contributing factor to the ecological vulnerability of mining areas [6]. Ground subsidence is a regional geological hazard that is common in mining areas [7]. It has the characteristics of being slow, progressive, and irreversible [8], and may endanger mining operations and human life. Therefore, it is crucial for both research and practical purposes to monitor ground subsidence in mining areas to obtain spatiotemporal information and make predictions, to provide data reference and technical support for environmental safety management in mining areas.

Leveling and the Global Positioning System (GPS) are examples of traditional geodetic systems that have strong observation accuracy across significant expanses of difficult terrain, but they also have drawbacks including single point observation, poor spatial resolution, and expensive costs [9]. With its benefits of great range, high precision, high

density, and cheap cost, time-series interferometric synthetic aperture radar (TS-InSAR), represented by permanent scatterer interferometry, may address the disadvantages of existing measuring methods [10,11]. Berardino and Lanari et al. [12,13] suggested a TS-InSAR approach based on multi-master pictures called small baseline subset interferometric synthetic aperture radar (SBAS-InSAR). By extracting surface deformation information using only interferometric pairs with short spatial and temporal baselines, it is possible to successfully prevent the effects of spatiotemporal decorrelation on the result [14]. Many research projects are now being conducted on the use of the SBAS-InSAR technology to measure ground subsidence in mining areas. Dey et al. [15] used SBAS technology to effectively obtain subsidence information for the Jharia coalfield in India from 2011 to 2016; Karamvasis et al. [16] discussed the advantages and disadvantages of TS-InSAR technology applied in mining areas; based on the enhanced SBAS-InSAR technique, Chen et al. [17] gathered data on significant gradient surface deformation in mining areas. The accuracy of SBAS-InSAR techniques in mining applications is also discussed [18]. All the above investigations show that the SBAS-InSAR approach may give significant support for monitoring ground subsidence in mining regions. Furthermore, the selection of SAR data is an important aspect influencing ground settlement monitoring outcomes. The key data sources in the analysis are presently ENVISAT [19], TerraSAR-X [20], COSMO-SkyMed [21], TanDEM-X [22], Sentinel-1 [23], ALOS [24], and Gaofen-3 [25]. Combining the features of Sentinel-1A data such as large observation range, high temporal resolution, and free access [26], this study uses Sentinel-1A data for SBAS-InSAR processing.

Physical models [27,28], mathematical statistical models [29,30], and artificial intelligence models [31,32] are the most often utilized approaches for predicting ground subsidence presently. The physical model for subsidence prediction is primarily based on the physical mechanisms of subsidence, including groundwater activity and changes in soil structure [33,34], simulated through an evolutionary process. The efficacy of this model is dependent on calibration and validation using actual measurement data [35]. In practice, such models are often constrained by the requirement for complex assumptions to be met, which can pose significant challenges for practical applications [36]. In contrast, the method of mathematical statistics has easy access to data and simple parameter definition. The method relies on the use of historical data to establish mathematical relationships to fit changes in sedimentation, mainly using time-series functions to provide predictions [37]. However, the method frequently lacks a physical and geological basis, making accurate prediction results for data with complicated rules and considerable fluctuations difficult to acquire [38]. Compared with the above two methods, the artificial intelligence method is not constrained by complex geological and hydro-physical parameters. It learns and fits ground subsidence patterns by constructing feature processes, model training, and regression prediction. Existing approaches for subsidence prediction include support vector regression (SVR) [39], artificial neural networks (ANN) [40], and Bayesian networks [41]. Although many studies have been developed in the field of ground settlement prediction research, the majority of them are still combined with traditional measurement techniques and primarily address the problem of reflecting ground settlement in small areas, with relatively few used in the prediction of time series of ground subsidence over large areas with high observation density. Long-short term memory (LSTM) is a network that processes sequential data and has a distinct advantage in processing time-series data, which corresponds exactly to SBAS-InSAR results. To train the prediction model, the algorithm also requires large sets of labeled data, which synthetic aperture radar interferometry can provide. Furthermore, empirically, the dependency of subsidence on information at different times is different, and the more comparable the time influence is, the more significant it is, and the original LSTM model does not take this into account adequately. Focusing on the input sequences and exploring the intrinsic connections between them, the attention mechanism [42] selectively weights the information features to improve the accuracy and efficiency of the model by discriminating the more critical information for the prediction results. Although widely adopted in computer vision and text classification,

its application and potential in ground subsidence prediction studies have not been fully explored, and thus merit further research [43]. Accordingly, this manuscript introduces an efficient spatiotemporal forecasting tool, dubbed as attention-based LSTM (AT-LSTM), for analyzing ground subsidence in mining regions. The proposed method is based on SBAS-InSAR data and consists of an LSTM network as the fundamental unit, along with an attention mechanism that accounts for subsidence characteristics in various temporal states.

The Pingshuo mine, which was established in the 1980s and is a major coal base in China, is highly mechanized and has comparatively comprehensive production security and living amenities [44]. Long-term mining has caused serious environmental problems in this mining area, with prominent ground subsidence, and scientific monitoring and protection are urgently needed [45,46].

Following are the precise goals of the current article: (1) to analyze Sentinel-1A remote sensing image data for the Pingshuo using SBAS-InSAR technology and obtain information on ground subsidence for 2019–2022; (2) to explore the spatial and temporal distribution of ground subsidence in the research region; and (3) to establish the AT-LSTM model based on InSAR time-series data for the spatiotemporal prediction of ground subsidence in mines, and to assess the model accuracy.

2. Materials and Data Processing

2.1. Study Area

The Pingshuo mining region is situated in the Pinglu District of Shuozhou City in the northern Shanxi Province of China, bordering the 'Black Triangle' of Jin, Shaanxi, and Mongolia, with a geographical area of 112°10′–113°34′E, 39°23′–39°37′N. The research region is part of the loess hilly terrain and is situated in the eastern portion of the Loess Plateau. The topography is high in the north and low in the south. The terrain is dominated by mountains and hills, which have an average elevation of roughly 1400 m. The region experiences a typical northern temperate semi-arid continental monsoon climate, with a year-round average temperature of 4.8 to 7.5 °C and 428.2 to 449 mm of precipitation. The surface water system in the study region is underdeveloped, and the Maguan River and Qili River, belonging to the Sangan River basin, are the main rivers. The hydrogeological conditions are relatively simple with low groundwater levels and weak water content. The aquifers in the area consist mainly of Ordovician-carbonate karst aquifers, Carbonifer-Permian clastic fracture aquifers and Fourth Series loose rock-like pore aquifers. They are primarily recharged by atmospheric precipitation and seepage water from mountain river beds during the rainy season. The mining activities and surface water interception have led to a significant reduction of surface water in the mining area as well as a substantial loss of stored groundwater.

The study area contains three large open-pit mines, Antaibao (ATB), Anjialing (AJL), and Donglutian (DLT), as well as three large modern underground mines, Jinggong-1 (JG-1), Jinggong-2 (JG-2), and Jinggong-3 (JG-3), as shown in Figure 1, which are typical open-underground combined mining. It is presently one of the largest and most advanced coal producing bases in China [47]. The three opencast mines ATB, AJL, and DLT are known to have come into production in 1985, 1998, and 2006 respectively [48], with the three underground mines put into operation between 2003 and 2007. For more than three decades, the ecological environment of the mines has been fragile and geological hazards have been a serious problem under the influence of a variety of natural and man-made factors [49]. After field investigation, it was found that there are several ground subsidence phenomena in the study area, which have a certain impact on the living and production activities in the region, as shown in Figure 2.

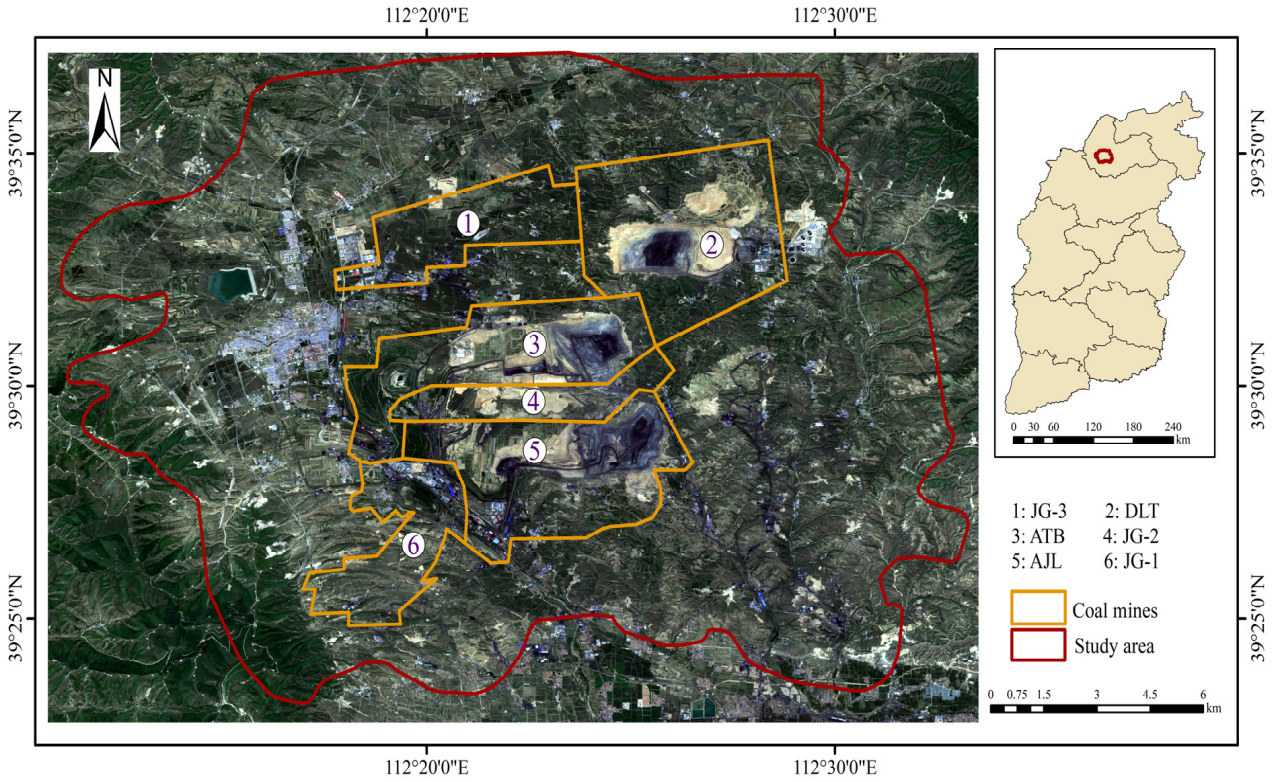

Figure 1. Location of the study area (Sentinel-2, 2021).

Figure 2. Photographs of ground subsidence sites in the study area.

2.2. Data

The SAR data used in this study are the single look complex (SLC) data products from the Sentinel-1A satellite with 37 scenes covering the study area under the interferometric wide (IW) swath model. The acquisition period is 2019–2022, with a maximum time baseline of 1165 days. Table 1 displays the primary parameters. Auxiliary data include precise orbit ephemerides (POD) and 12.5 m-resolution DEM data provided by the ALOS (Advanced Land Observing Satellite) satellite.

Table 1. Sentinel-1A data detail.

Parameter	Sentinel-1A
Band	C
Direction of orbit	Ascending
Track number	113
Incidence angle/°	39.16
Azimuth/°	346.55
Polarization mode	VV
Spatial resolution/m	5 × 20
Period/d	12
Date range	2019.01.20–2022.03.29
number of SLCs	37

2.3. SBAS-InSAR

The differential interferometry synthetic aperture radar (D-InSAR) technology is modified in SBAS-InSAR [13]. It utilizes shorter temporal and spatial baselines to acquire a greater number of interferogram pairs, which help to preserve the coherence of the interferograms. Phase unwrapping is applied to each interferogram that is generated. The method combines all SAR images into a number of sets, which are collections of short temporal and spatial baselines. The surface deformation within each subset is calculated based on the least squares method, and the singular value decomposition (SVD) method is used to solve the rank deficiency problem of the overall normal equation. Small baseline sets are solved jointly, where the baseline distances are small within the set and relatively large between sets. In order to solve the problem of delayed atmospheric phase caused by spatial and temporal decoherence, high-quality determination of coherence points and high-accuracy image matching are required.

One of the N + 1 SAR images acquired covering the same region is chosen as the primary image, and the rest of the images are registered with it. M interferograms are generated by combining them. Then, M satisfies:

$$\frac{N+1}{2} \leq M \leq \frac{N(N+1)}{2} \tag{1}$$

For the ith pair of interferograms generated from the two images acquired at moments t_A and t_B, the interference phase at any point of the image is expressed as:

$$\begin{aligned} \Delta\varphi_i &= \varphi_B - \varphi_A \\ &\approx \tfrac{4\pi}{\lambda}(R_B - R_A) + \Delta\varphi_i^{atm} + \Delta\varphi_i^{topo} + \Delta\varphi_i^{n} \end{aligned} \tag{2}$$

In the above equation, λ is the wavelength, R_A and R_B are the cumulative shape variables in the line of sight (LOS) at moments t_A and t_B, respectively. $\Delta\varphi_i^{atm}$, $\Delta\varphi_i^{topo}$ and $\Delta\varphi_i^{n}$ represent the phase errors due to atmosphere, elevation, and noise, respectively.

SBAS-InSAR data processing was carried out in this investigation utilizing SARscape on the ENVI 5.3 platform, and the process is shown in Figure 3. The main operational steps are connection graph generation, differential interferogram generation, orbit refining and re-flattening, SBAS inversion, and final geocoding.

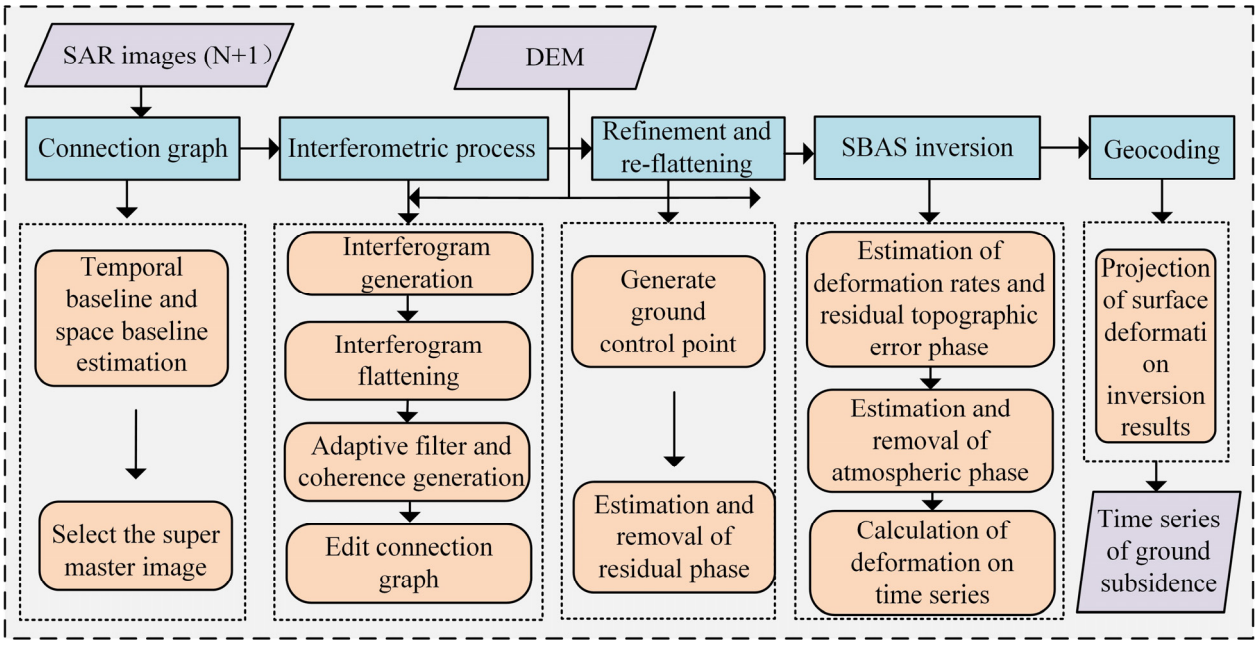

Figure 3. SBAS-InSAR basic processing flow.

First, the images of the data were estimated based on the thresholds of the temporal and spatial baselines, and the 18 August 2020 image was selected as the super master image (Figure 4). Then, it was registered with other images, and the differential interferogram and unwrapping image were obtained by removing the terrain phase, interference processing, and phase unwrapping. Residual phases were removed by orbit refinement and re-flattening using DEM. After that, the deformation rate and elevation error were estimated using SVD, and the atmospheric phase was estimated and removed by temporal high-pass filtering and spatial low-pass filtering. Finally, the surface deformation inversion results were geographically projected and the LOS directional deformation results converted into vertical results using the following Equation (3).

$$d_v = \frac{d_{LOS}}{cos\theta} \tag{3}$$

where d_v is the vertical deformation results, d_{LOS} is the LOS deformation results, and θ is the angle of radar incidence.

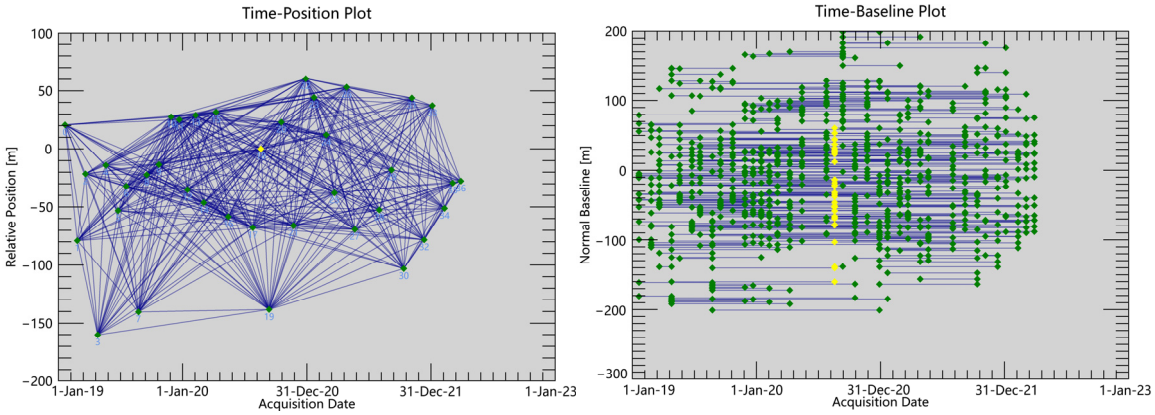

Figure 4. Spatial-temporal baseline distribution.

2.4. Wavelet Analysis

Wavelet analysis is a widely used method for time-frequency analysis that can reveal the hierarchical and periodic features of signals across various time scales [50]. In this study, we employed Morlet continuous wavelet analysis to analyze the time-series period of ground subsidence in mining areas. The resulting analysis provided valuable guidance for selecting optimal parameters for our prediction model. Mathematically, the Morlet continuous wavelet analysis can be can be defined as the product of a complex sine wave and a Gaussian window [51]:

$$\psi = e^{2i\pi ft} e^{-\frac{t^2}{2\sigma^2}} \tag{4}$$

$$\sigma = \frac{n}{2\pi f} \tag{5}$$

where i is the imaginary operator, f is the frequency, and t is the phase time. σ is the standard deviation of the Gaussian function.

The wavelet coefficients are as follows:

$$\xi(t', a) = a^{-\frac{1}{2}} \int f(t) \psi^* (\frac{t}{a} - \frac{t'}{a}) dt \tag{6}$$

where *f(t)* is the subsidence time series, ψ^* is the conjugate function of ψ, a is the scale factor of the wavelet transform (Stretch factor), and k is the coefficient.

3. Surface Subsidence Prediction Model

Leveraging the strengths of LSTM in time-series data feature learning and the ground subsidence time-series results obtained from SBAS-InSAR inversion, this study proposes an attention-based LSTM ground subsidence prediction model, termed AT-LSTM, as depicted in Figure 5. The model comprises five key modules: the input layer, hidden layer, attention module, model training, and output layer. The input layer is the model data preprocessing stage, which prepares the initial time-series data to satisfy the network input specifications. The output layer then offers the final prediction results by iterating them point-by-point. The hidden layer is a recurrent neural network (RNN) built from LSTM cells, and the attention module is weighted to optimize the outcomes of the LSTM output process. The adaptive moment estimation (ADAM) algorithm is used to optimize the model parameters during the training phase.

3.1. Data Preprocessing

Time series are collections of numerical, continuous data that record observations of processes and are frequently viewed as a whole [52]. To improve the quality of the training samples, the time-series data of ground subsidence in the study area needed to be preprocessed, including data cleaning, normalization, and sample division. Due to a certain degree of decoherence in the mine area, NAN values existed in the SBAS-InSAR processing results, which we removed, and to reduce the introduction of errors, the blank area was no longer supplemented.

For the raw time-series data $X = \{x_1, x_2, x_3, \ldots, x_i, \ldots x_n\}$, the settling sequence at each point is denoted $x_i = (x_1, x_2, x_3, \ldots, x_t, \ldots x_T)$. Lowess (locally weighted scatterplot smoothing) was used for noise reduction and smoothing. The maximum-minimum normalization method (Equation (4)) was used to normalize the data to remove the dimensional influence and produce $X' = \left\{x_1', x_2', x_3', \ldots, x_i', \ldots x_n'\right\}$, which was divided into an 80% training set $X'_{train} = \left\{x_1', x_2', x_3', \ldots, x_i', \ldots x_m'\right\}$ and 20 % test set $X'_{test} = \left\{x'_{n-m+1}, x'_{n-m+2}, \ldots, x_i', \ldots x'_n\right\}$.

$$x_i' = (x_t - x_{imin}) / (x_{imax} - x_{imin}) \tag{7}$$

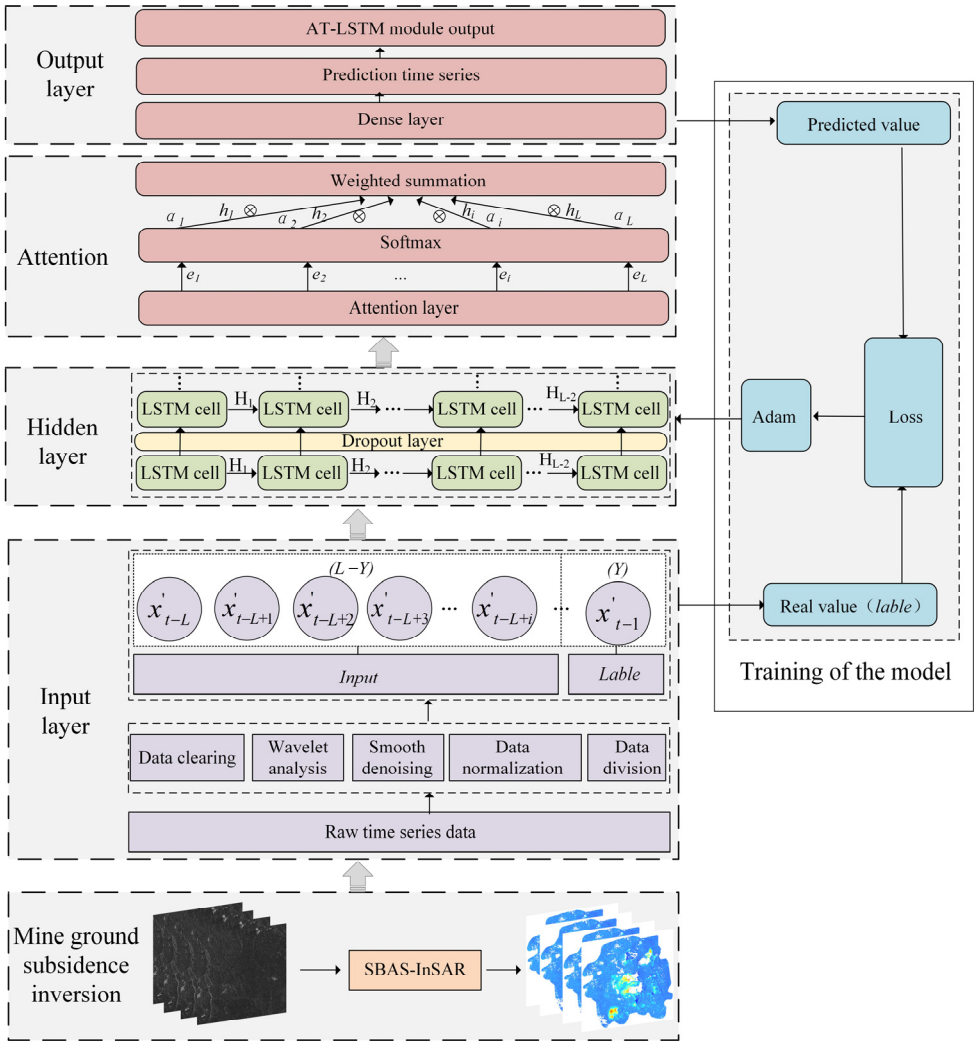

Figure 5. AT-LSTM ground subsidence prediction framework.

Time-series data prediction is the use of historical data to predict the most likely values at subsequent moments [53]. To determine the optimal historical series length, this study used wavelet analysis of the periodic variation of mine subsidence sequences to provide a reference for the selection of sequence length in the AT-LSTM model. The dataset was divided using a sliding window. According to a parametric historical time series of controllable length L, a training sample $x_{\text{train}}{}' = \left(x'_{t-L}, x'_{t-L+1}, x'_{t-L+2}, \ldots, x'_{t-L+i}, \ldots x'_{t-1}\right)$ is retrieved. The initial L-Y data are utilized as sample inputs, and the last Y data are sample labels. L and Y satisfy the criteria $2 \leq L < T$, $1 \leq \mathrm{Y} < L$.

3.2. Long-Short Term Memory Network

In order to successfully combat the gradient disappearance issue in a recurrent neural network (RNN), a long-short term memory (LSTM) network is used to incorporate a "gate" mechanism in the hidden layer and then dynamically change the backpropagation procedure. It is a particular variety of convolutional neural network [54]. Compared with general RNN models, the unique structural design of LSTM avoids the problem of long-term dependency and can learn long-range time-series data [55]. The cell state and numerous gate topologies of the LSTM make up its core principle. The cell state, which may be thought of as the "memory" of the network, is analogous to a channel that communicates pertinent information along the sequence chain and stores previous data and long-term states. Cell states might theoretically provide significant information during the whole

sequence processing. In light of this, the impact of short-term memory is diminished, since information learned at an earlier step can also be transmitted to cells at a subsequent time step. During the training process of the network, information can be added or removed through gates, which in turn control the flow of information. The LSTM consists of several hidden cells, and its cell structure is shown in Figure 6 below.

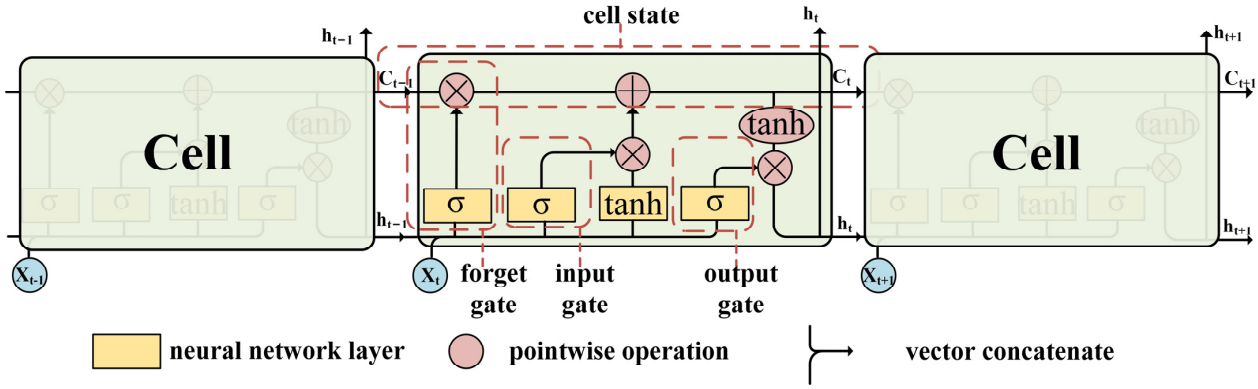

Figure 6. Cell structure of LSTM hidden layer.

As illustrated in Figure 6, the hidden layer consists of three LSTM cells, each incorporating three gate structures: input gate, forget gate, and output gate. These gates allow the LSTM to update and store data. Specifically, gate structures are constructed using sigmoid functions and bitwise multiplication operations; the gate itself does not introduce additional information. The generic representation for gates is as follows:

$$g(x) = \sigma(Wx + b) \tag{8}$$

The nonlinear activation function $\sigma(x) = 1/(1 + exp(-x))$, often known as the sigmoid function, is frequently employed in machine learning. It may be used to map a real number to the range of 0 to 1, and it is used to express how much information is sent. Information cannot travel through the gate if its output value is 0, but it may if it is 1, in which case all information is permitted to do so. W stands for the weight matrix, and b stands for the bias, with x_t and h_t denoting the input and corresponding hidden state output at moment t in the sample time series, respectively. Input gate, forget gate, cell state, and output gate are represented as i, f, c, and o, respectively. The LSTM carries out data input, information forgetting, cell state updating, and implicit state output in each cell in turn, and its forward computation process can be expressed as Equations (6)–(10).

How much of the current input data x_t to the network travels into the memory cell, or how much may be stored, is controlled by the input gate:

$$i_t = \sigma(W_{xi}x_t + W_{hi}h_{t-1} + b_i) \tag{9}$$

The self-linking cell is under the control of the forget gate, which also has the power to select which portions of the past data will be ignored. That is, how much of the data from the memory cell c_{t-1} from the previous moment has an effect on memory cell c_t at this particular time, t.

$$f_t = \sigma(W_{xf}x_t + W_{hf}h_{t-1} + b_f) \tag{10}$$

$$c_t = f_t c_{t-1} + i_t \tanh(W_{xc}x_t + W_{hc}h_{t-1} + b_c) \tag{11}$$

The current output value h_t is controlled by the output gate in relation to the memory cell c_t. Equation (8) shows the value of the output gate, while Equation (10) gives the h_t produced by the LSTM cell at the instant moment t.

$$o_t = \sigma(W_{of}x_t + W_{of}h_{t-1} + b_o) \tag{12}$$

$$h_t = o_t \tanh_c(c_t) \tag{13}$$

3.3. Attention Mechanism

Attention mechanisms enable neural networks to selectively attend to a subset of inputs (or features) to improve their task performance. By prioritizing resource allocation to more important tasks, attention mechanisms facilitate importance assessment and trade-offs of information processing, especially in the context of limited computational resources.

The subsidence state of each moment, as well as the hidden state and memory value of the final output, can be obtained when the input time series is output from the last layer of the LSTM. The mining environment is intricate, and information received at various times has varying implications on the state prediction at a particular time. In order to reduce the model prediction error by boosting the importance of key time steps in the LSTM, an attention mechanism is incorporated to assess the significance of the information generated at various points in time. To reduce network parameters and computational burden while maintaining temporal information, we propose introducing a fully connected layer between the hidden and output layers of the original LSTM network based on the attention mechanism. The objective is to weight and sum the outputs of multiple hidden neurons at each time step through this layers' operation.

The proposed approach involves the following steps: firstly, utilizing the output vector of the final LSTM hidden layer as the input to the attention layer, which is trained using a fully connected layer. Afterwards, the softmax function is applied to normalize the output of the fully connected layer, which yields the weight assigned to each hidden layer vector. The magnitude of each weight reflects the importance of the corresponding hidden state for prediction at each time step. The weight training process is carried out as follows:

Taking the sequence of state features $H^t = (h_1, h_2, h_3, \ldots, h_i, \ldots, h_L)$, output from the last layer of the LSTM, as input to the attention mechanism, we define:

$$e_i = \tanh(W_h h_i + b_h) \tag{14}$$

$$\alpha_i = \frac{\exp(e_i)}{\sum_{i=1}^{L} \exp(e_i)} \tag{15}$$

where e_i is the importance of the ith feature at moment t, calculated by building a layer of the simple neural network, and W_h and b_h are the network learning parameters. α_i is the feature weight. The final model output, i.e., the weighted feature sequence, is obtained as follows:

$$S^t = \sum_{i=1}^{L} \alpha_i h_i \tag{16}$$

3.4. Model Training

The network training took the hidden layer as the core. The LSTM was initialized with 2 layers and the dropout layer was used to suppress overfitting during the network training. The model optimizer was Adam, an algorithm that incorporates the operational advantages of AdaGrad in sparse gradients and RMSProp in online and non-stationary environments, is well suited to problems with large data and/or parameters, runs efficiently, and performs better than other methods [56].

The time-series data of the hidden layer input was a two-dimensional array of (m, L-Y), and the sample labels and outputs were both two-dimensional arrays of (m, Y). The MSE was used as the error statistics criteria, and the loss function during training was specified as follows:

$$loss = \frac{1}{n} \sum_{i}^{m} \left(x'_{pred} - x'_{real} \right)^2 \tag{17}$$

In network training, weights and biases are adjusted until a user-defined stopping condition is met. When the error-epoch curves of the training and test sets converge, the trained model is considered valid in this study.

In the training of the LSTM prediction model, the minimum loss function is set as the optimization goal, and the network is iteratively updated by setting parameters to obtain the trained model. These parameters include time step (L), number of network layers (S), number of neurons in the hidden layer (F), learning rate (l), epochs and dropout.

3.5. Model Prediction and Evaluation

For the trained AT-LSTM prediction model, input the prediction data $X'_{pred} = \left\{x_1', x_2', x_3', \ldots, x_i', \ldots x_n'\right\}$, and output the prediction result $Y'_{pred} = \left\{y_1', y_2', y_3', \ldots, y_i', \ldots y_n'\right\}$ through the full connection layer. Inverse normalize the predicted values to obtain the final ground subsidence prediction result $Y_{pred} = \{y_1, y_2, y_3, \ldots, y_i, \ldots y_n\}$. The calculation formula is as follows:

$$y_i = y_t'(x_{imax} - x_{imin}) + x_{imin} \tag{18}$$

This study measures the accuracy of the developed subsidence prediction model using mean square error (MSE) and mean absolute error (MAE), computed as follows.

$$MSE = \frac{\sum_{i=1}^{n}(y_i - \hat{y}_i)^2}{n} \tag{19}$$

$$MAE = \frac{\sum_{i=1}^{n}|y_i - \hat{y}_i|}{n} \tag{20}$$

where n indicates the number of points in the prediction set, and y_i and $\hat{y}_i$ represent the predicted and actual values of subsidence at point i.

4. Results and Discussion

4.1. Spatiotemporal Analysis of Ground Subsidence in the Mining Area

Based on 37 ascending track Sentinel-1A images, the annual average vertical directional subsidence rate of the mine area from 2019 to 2022 was obtained using the SBAS-InSAR technique, as shown in Figure 7 below. It was evident that the loss of coherence in the three open-pit mining regions of AJL, ATB, and DLT was severe and that no data on subsidence could be acquired. The findings demonstrate the clear presence of the subsidence phenomena in the mine region. The maximum vertical directional subsidence rate is −205.89 mm/yr, and the maximum uplift rate is 59.70 mm/yr, with an average value of −4.50 mm/yr, and the subsidence exhibits a specific spatial aggregation distribution.

The accuracy of SBAS-InSAR results was verified using level data and comparison with existing research results. The error of the monitoring results compared with the level data was 8.36 mm, and the spatial distribution of subsidence was consistent with the results of the studies based on D-InSAR and StaMPS-SBAS [57,58]. The findings of this study are therefore reasonably trustworthy and can be applied to ground subsidence prediction research in the mining area.

As depicted in Figure 7, the mine area exhibits three distinct subsidence zones. (1) The JG-1 mining area: Underground mining activities disrupt the original mechanical equilibrium state of the rock body surrounding the mining area, causing the rock layer to move, deform, and ultimately be destroyed. As mining operations progress, these movements spread to the surface and contribute to settlement. Gradually, the subsidence process becomes increasingly evident, forming a subsidence basin, which is the most severe subsidence area in the mining region. (2) The west side of the ATB and AJL open-pit mines with

a subsidence rate of up to 70 mm/yr: This area is characterized by a complex environment, featuring staggered shaft mines and open-pit mines. The mining activities in the shaft mines can impact the open-pit mining and lead to settlement in the end gang or discharge field. (3) The dumping site located in the northeast area of the DLT open-pit mine, which exhibits a settlement rate of approximately 50 mm/yr: Dumping refers to the process of discharging stripped material from the open pit into a designated location. In this case, the dump site mainly consists of artificially accumulated loose objects that are susceptible to settlement under the influence of various engineering activities. Additionally, there is a slight distribution of subsidence in the southeast of the research region, where it is understood that a few minor mines are located. The findings show that the mining operations and the subsidence process are closely associated.

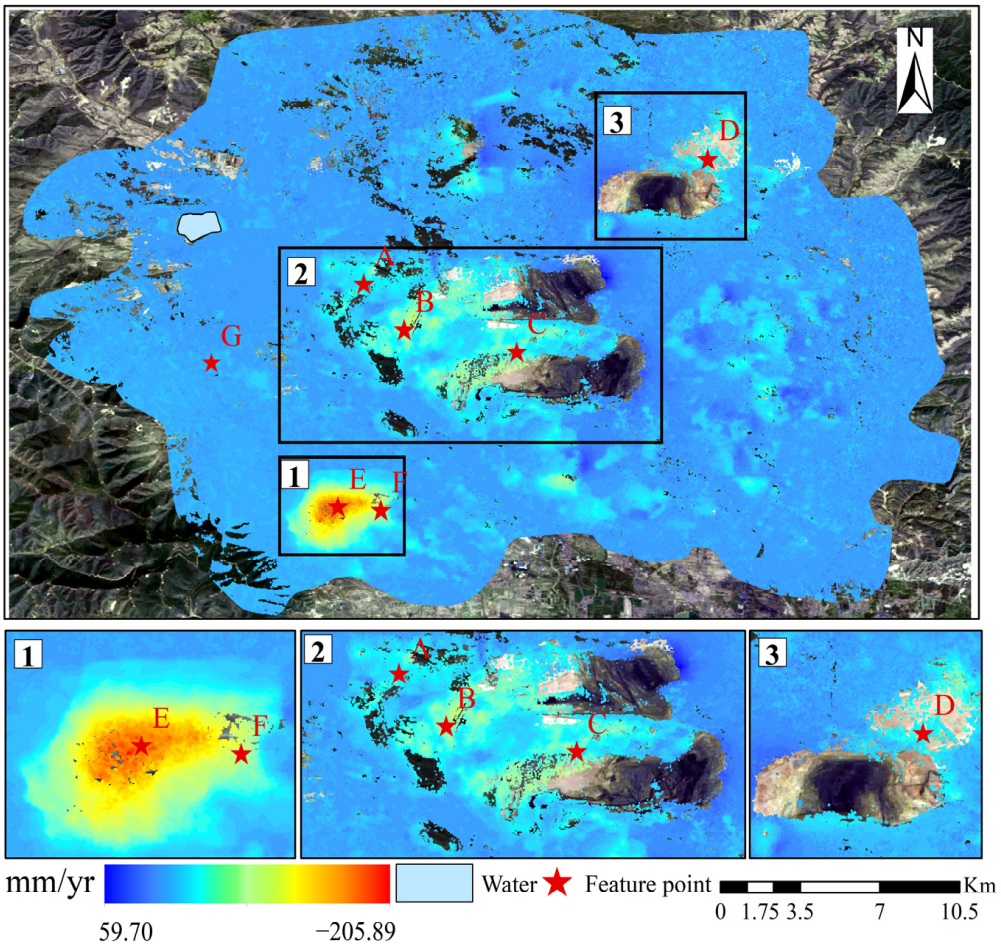

Figure 7. Average annual rate of ground subsidence at the mine area.

The uplifted area of the mine is primarily located along the direction of open-pit mining and is distributed at the edge of the mining pit. This phenomenon is mainly due to the gradual expansion of the mining area towards the edges during open-pit mining. As the coal strata beneath the ground gradually diminish, voids will form and expand, creating areas of unstable support that are prone to fracture and collapse, resulting in ground uplift at the edge of the mine area [59,60]. Additionally, during the open-pit mining process, a substantial amount of engineering activities, including excavation, blasting, and transportation, generates changes in the ground's stress state that can contribute to further ground uplift.

In Figure 7, A, B, C, D, E, and F are characteristic points located in three typical subsidence areas, respectively, and point G is a stable reference point. The temporal variation of the accumulated subsidence at these seven points is shown in Figure 8 below.

As a stable position with little variation over the course of the monitoring cycle, point G can be deemed to have no subsidence issues. The cumulative settlement of points A, B, C, D, E, and F generally maintains an increasing trend, but the nature and scope of changes at local moments are different. Points A, B, and C are located relatively close to each other, and the trend of change remains basically the same throughout the monitoring cycle. The final cumulative settlement is B, C, and A in descending order, and B and C exceed 100 mm. Point D displayed a pattern of lifting initially before settling, and at a later time, the total settlement was very similar to that of point A. While both Points E and F are located within the subsidence basin, Point E is more closely situated to the center of the basin. For the first 180 days or so (until 19 July 2019), the subsidence amounts at the two points were roughly synchronized. After that, the subsidence rates started to differ, the increase at point F became slower, and the gap between the subsidence amounts at the two points grew until, at its culmination, the cumulative subsidence amount at point E was close to 500 mm, while that at point F was close to 250 mm, a much smaller amount than that at point E.

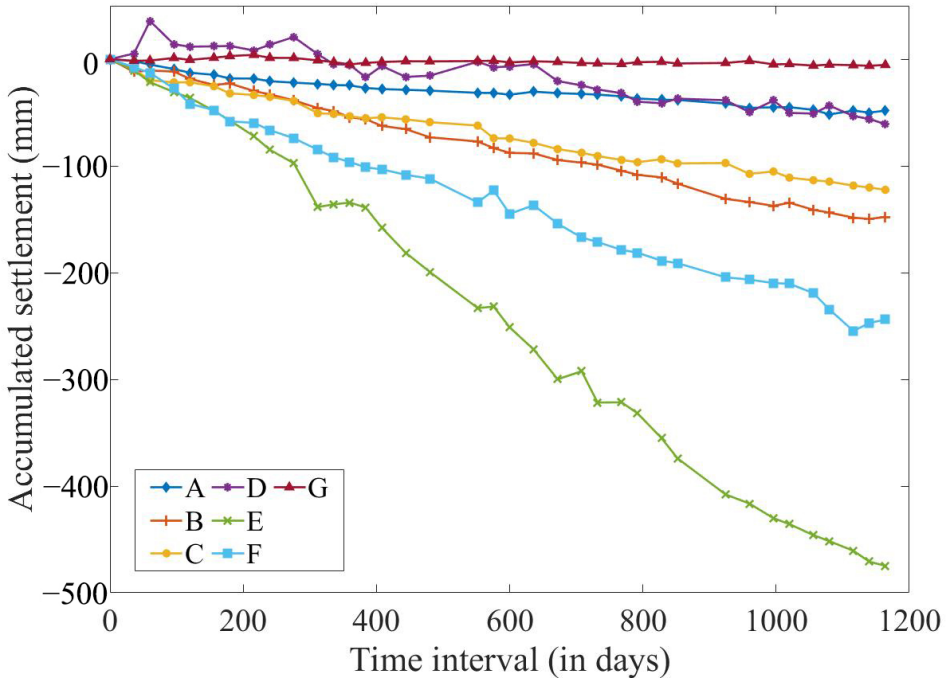

Figure 8. Time series of feature point subsidence.

Figure 9 displays the time-series deformation of the mining area over the monitoring cycle from 2019 to 2022. The spatial and temporal variations in ground subsidence within the study region are unevenly distributed and notably pronounced. These fluctuations exhibit a strong correlation with mining activity. Ground subsidence increases most rapidly within the JG-1 area, gradually expanding from east to west and consistent with the direction of underground mining. This area also experienced the most severe subsidence throughout the study region. The increase in subsidence around the ATB and AJL open pits was relatively slow, with subsidence starting to become apparent in 2020 and becoming more pronounced and extending from east to west in 2021, in line with the direction of open-pit stripping, with a continuous area of subsidence clearly visible by 2022. In contrast, the northeastern part of the DLT shows less variation in the rate and extent of subsidence than in other mentioned areas, though still experiencing marked subsidence (<−125 mm) during the latter part of the monitoring cycle.

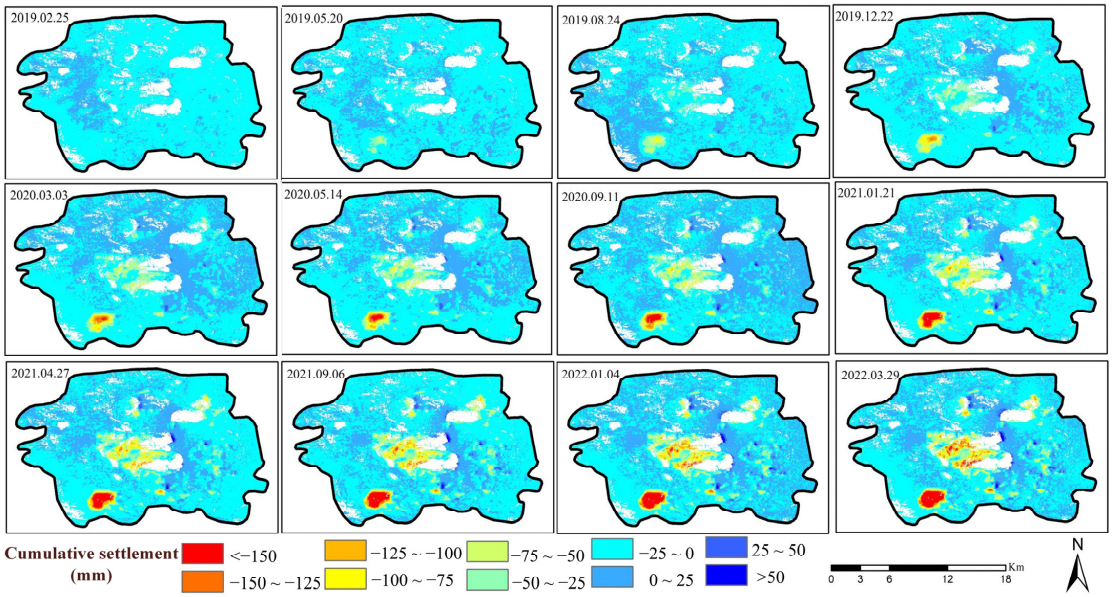

Figure 9. Spatial and temporal variations in ground subsidence in the study area.

4.2. Model Prediction

4.2.1. Sample Division

Based on the above ground subsidence inversion results, the subsidence time-series data from the observation points were preprocessed to obtain a training sample with a capacity of 1,644,327. The key parameters for the division of the dataset are the historical series length (time step) L and the output length Y. Different L and Y values affect the accuracy of the model prediction results, so we used the error variation to determine these two parameters.

The subsidence period is analyzed using wavelet variation in Figure 10, indicating that the period of the subsidence sequence is approximately 18. As such, the time step ranges from 1 to 18. Figure 11 presents a heat map of the MAE change for various sample divisions (S is set to 3, and F is set to 32). The figure reveals that with consistent input time steps, the error gradually increases as the sample output length grows. Therefore, we confine the output length to a single step (i.e., Y is equal to 1) in the proposed model.

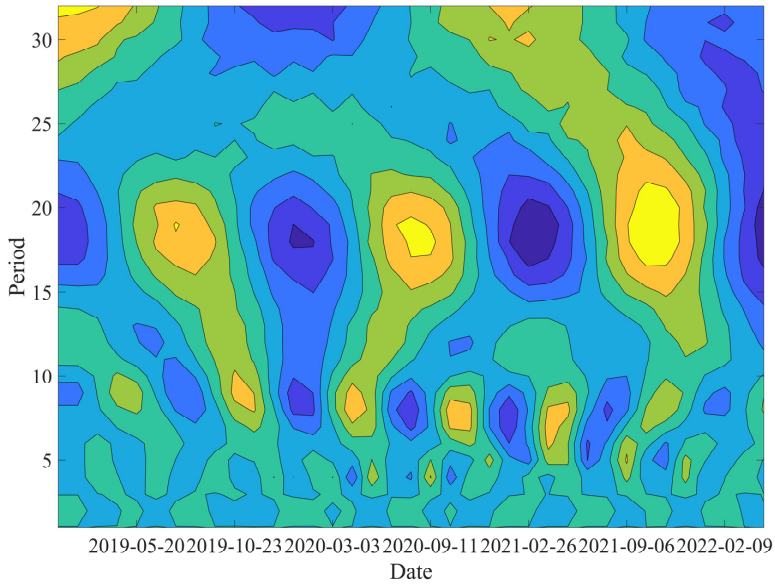

Figure 10. Periodic variation of subsidence.

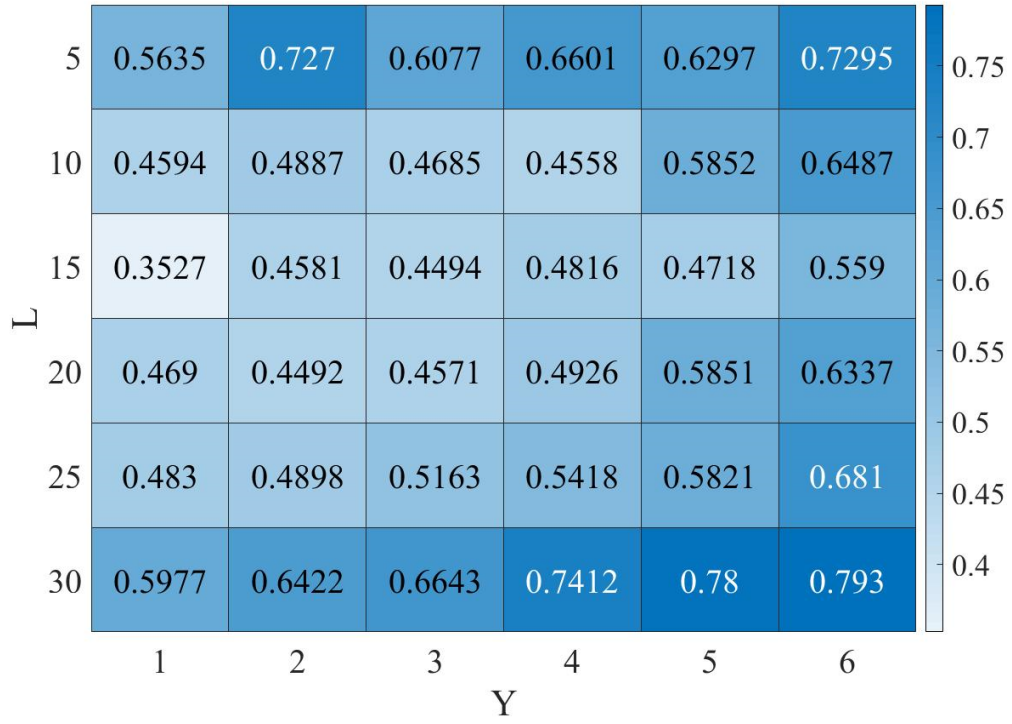

Figure 11. Selection of sample division parameters (S = 3, F = 32).

The error variation of the single-step prediction results at different time steps was further compared to determine the optimal L value, as shown in Figure 12. It can be noted that the error tends to decrease when $L < 9$, smooths out for $9 \leq L < 20$, and fluctuates for $20 \leq L$, indicating that it is not the case that a longer time-step length of the input has the better effect. According to the criteria for the selection of L with smoother error variation and lower error values, the most suitable time step length L = 16 was finally selected for this study.

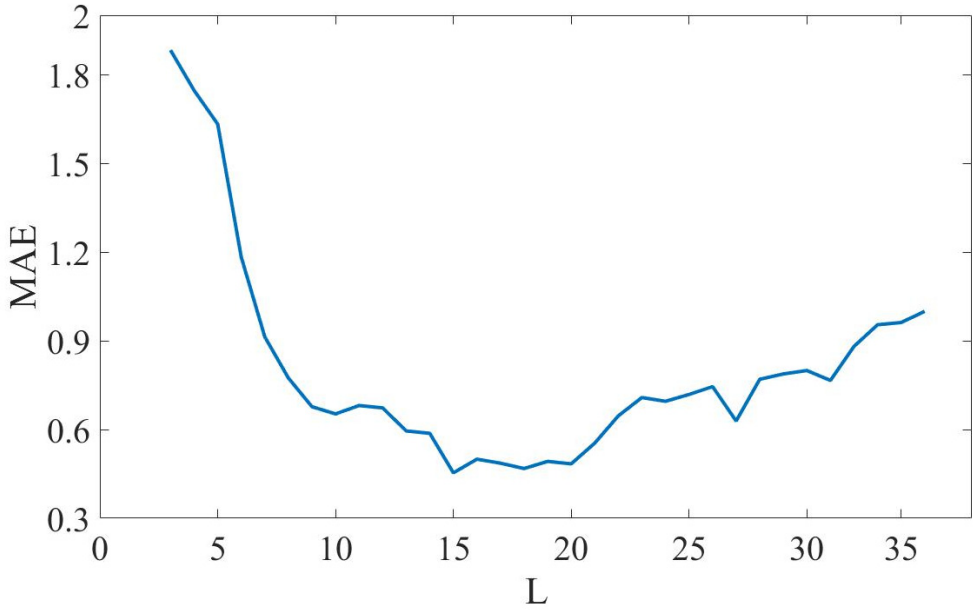

Figure 12. Variation of MAE at different time steps (S = 3, F = 32).

4.2.2. Network Parameters

A variety of hyperparameters, including time step L, number of network layers S, number of hidden layer neurons F, learning rate l, number of training epochs, and dropout, have an impact on the prediction model. L, S, and F are the most important of these. This study investigates the prediction effectiveness of the model with different network parameters S and F. Figure 13 below displays the single-step prediction accuracy results for the model with various parameters, with L = 30 as an example. It is demonstrated that although there was a high local correlation, the model prediction accuracy and model complexity were not necessarily positively connected [61]. For L = 30 and Y = 1, the optimal parameters were S = 3 and F = 24. After several debugging, the final combination of parameters for the LSTM prediction model determined in this paper is shown in Table 2 below. As can be noted from Figure 14, the loss convergence changed normally during the model training process, and the overfitting during the network training process was effectively suppressed. Therefore, the model constructed in this paper is an effective model.

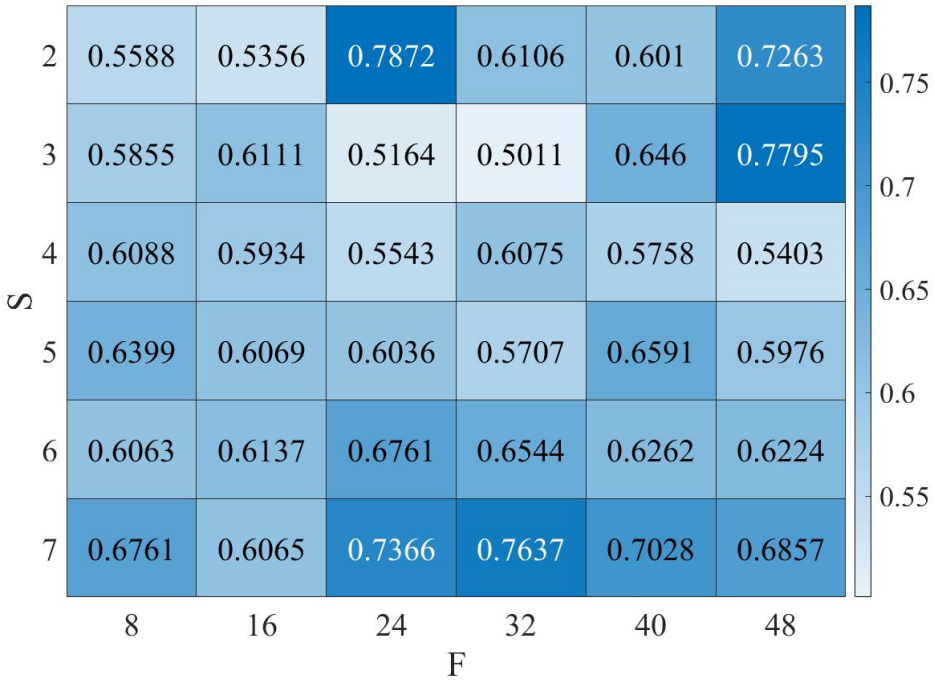

Figure 13. Network parameters selection (L = 30, Y = 1).

Table 2. Model parameters setting.

Parameters	Settings
Time step (L)	16
Output length (Y)	1
Number of hidden layers (S)	3
Number of neurons in the hidden layer (F)	32
Epochs	200
Loss function	MSE
Activation function	Tanh
Optimizer	ADAM
Batch size	512

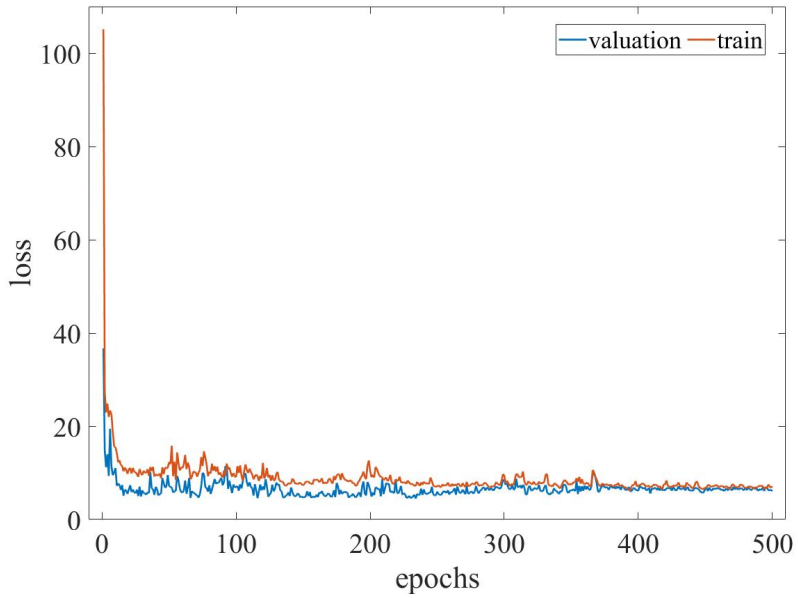

Figure 14. Variation of loss function value during AT-LSTM model training.

4.2.3. Prediction Results

Based on the aforementioned model parameters, the proposed AT-LSTM model was derived through training with data ranging from January 2019 to April 2020. To assess the efficacy of the model, four distinct data periods were randomly selected from the dataset for prediction, and the correlation between the predicted outputs and SBAS-InSAR monitoring outcomes is depicted in Figure 15 below. It can be seen that the correlation coefficient is above 0.97, indicating that the model prediction results have high accuracy and validity.

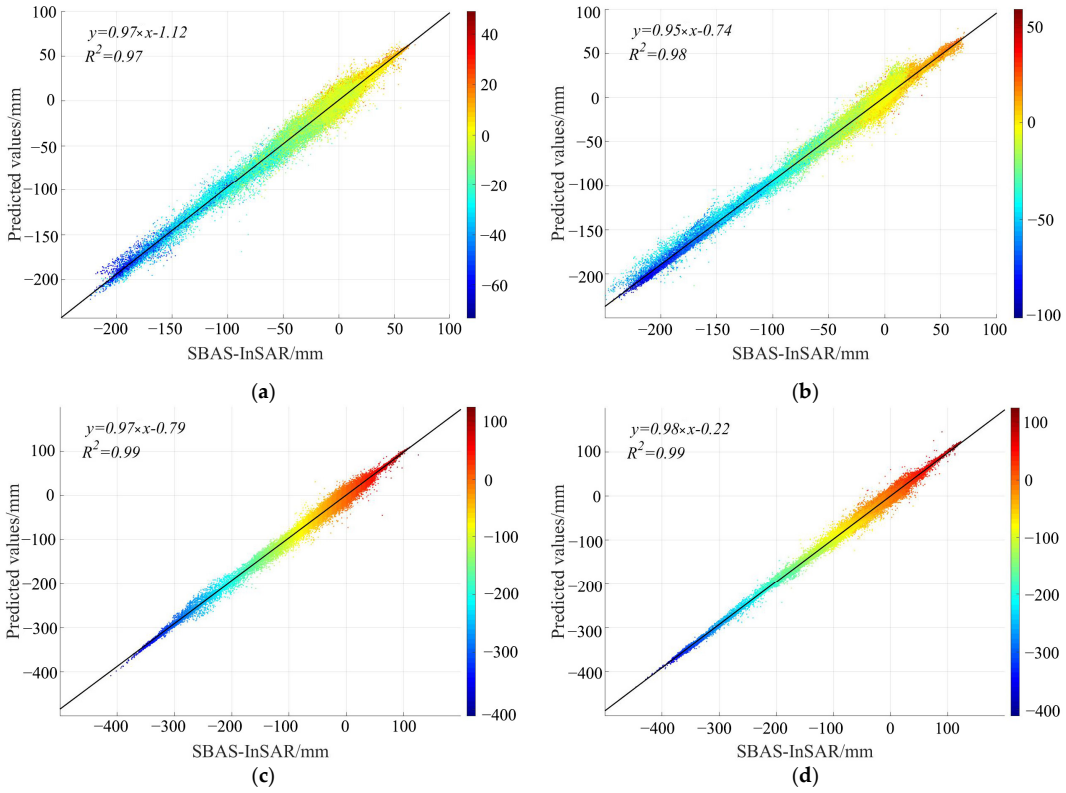

Figure 15. Correlation analysis of model prediction results. (**a**) 2020.08.18; (**b**) 2020.12.28; (**c**) 2021.09.06; (**d**) 2022.01.14.

Figure 16 presents the prediction results for six feature points (A–F) obtained by further analyzing the AT-LSTM model's performance on the time series. Combining the accuracy (Table 3), it is evident that the AT-LSTM model produced more precise predictions than the LSTM model, with relatively low prediction errors, with the lowest values being 0.71 mm and 2.16 mm^2, respectively. In general, it appears that the AT-LSTM model fitted the data better than the LSTM model and captured the local fluctuation changes of the time-series data more ideally (red dashed ellipse), indicating that the prediction model proposed in this paper has certain advantages and high credibility when dealing with ground settlement time-series data.

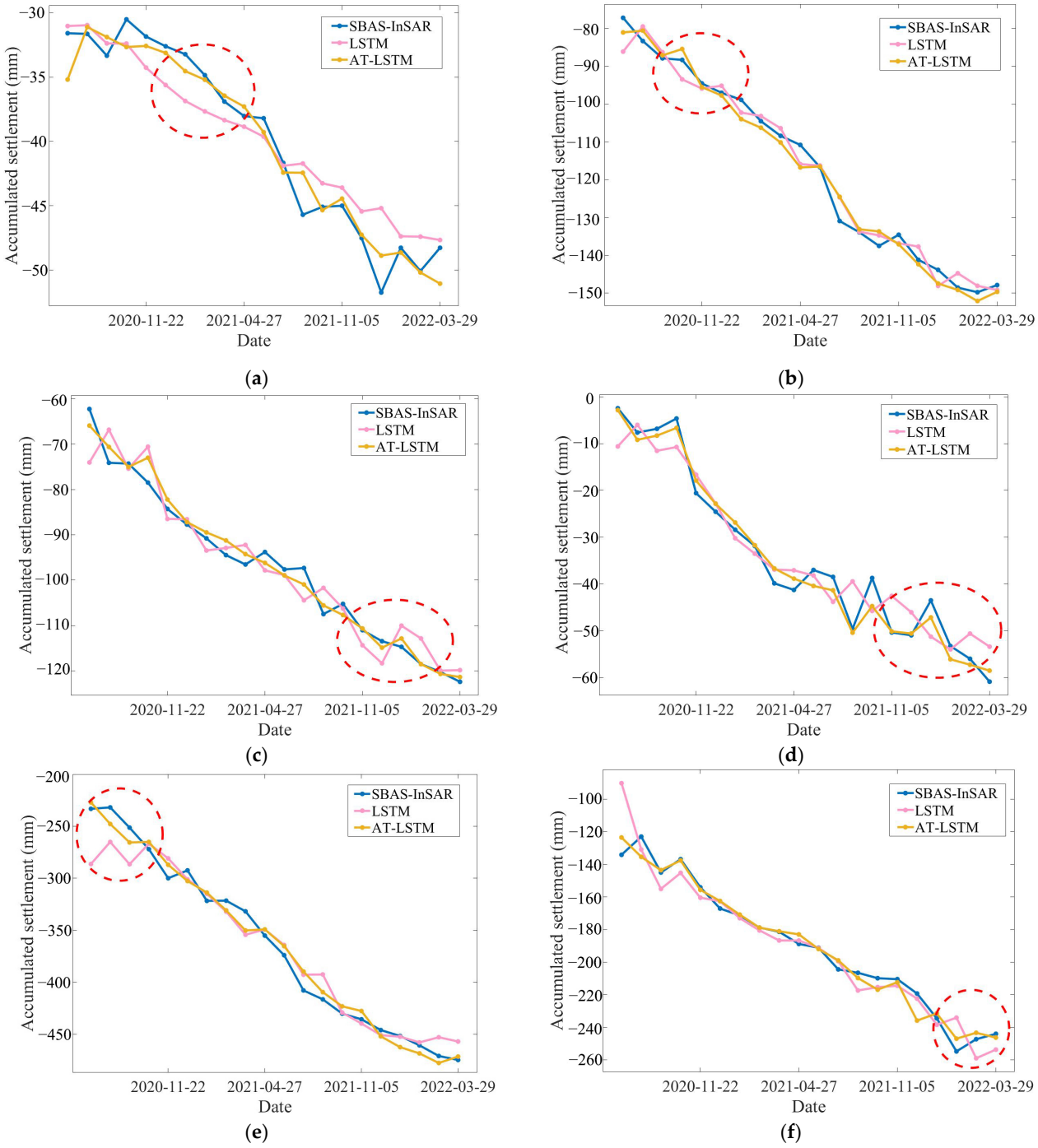

Figure 16. Time series for prediction of feature points A–F. (**a**) A; (**b**) B; (**c**) C; (**d**) D; (**e**) E; (**f**) F.

Table 3. Prediction accuracy of feature points.

	MAE/mm		MSE/mm^2	
	LSTM	**AT-LSTM**	**LSTM**	**AT-LSTM**
A	2.52	0.71	5.83	2.16
B	1.34	1.26	7.47	3.29
C	1.59	0.99	6.09	2.21
D	3.41	1.04	6.16	2.37
E	5.36	1.52	9.51	3.46
F	4.28	0.95	7.95	2.53

4.2.4. Distribution of Errors

To acquire the error spatial distribution, the AT-LSTM prediction results were superimposed with the SBAS-InSAR monitoring data (Figure 17). It is evident that the prediction errors are concentrated in ±2.0 mm, with mean MAE and MSE values of 0.94 mm and 2.20 mm^2, respectively.

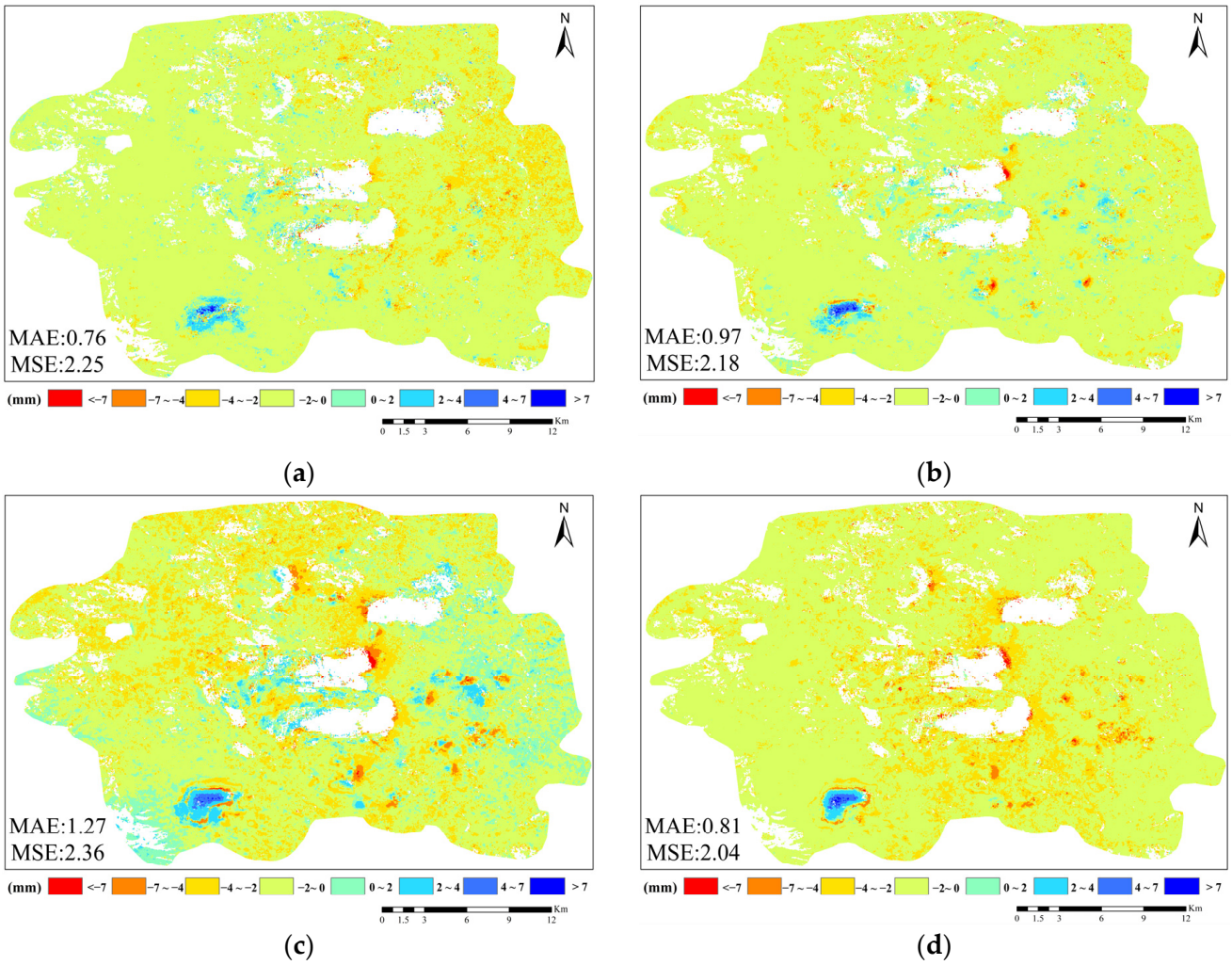

Figure 17. Spatial distribution of prediction errors. (**a**) 2020.08.18; (**b**) 2020.12.28; (**c**) 2021.09.06; (**d**) 2022.01.14.

Based on the mining operation in the coal mine, it was observed that the areas with prediction errors > 4 mm were mainly located in JG-1 and would extend with the expansion of the subsidence basin, while areas with prediction errors < −4 mm were distributed along the direction of the open-pit mine. This implies that the model is sensitive to the mining

method used in the mining area, with higher predicted values than actual values in the open-pit mine and vice versa in the shaft mine. Overall, the prediction results provided by the proposed model in this study show small deviations from the actual situation, and can objectively reflect the spatial patterns of surface settlement in the mining area. Therefore, the predicted results can be considered reliable.

4.3. Comparison of Prediction Methods

This study evaluated the performance of the AT-LSTM prediction model by comparing it with several other models, including Holt-Winters, autoregressive integrated moving average (ARIMA), support vector regression (SVR), gray model (GM (1,1)), RNN, and LSTM. To assess the accuracy (measured by MAE and MSE) and computational complexity (represented by the modeling time) of each model, the same dataset was used for comparison. The results of the study are presented in Table 4.

Table 4. Comparison of different prediction models.

Model	MAE/mm	MSE/mm^2	Modeling/Minutes
holt-winter	5.44	4.28	6.8
ARIMA	4.86	3.37	77.9
SVR	3.13	3.41	23.3
GM(1,1)	3.24	3.11	5.2
RNN	2.35	2.74	25.1
LSTM	1.28	2.58	30.5
AT-LSTM	0.73	1.96	32.6
Computer configurations	Processor: Intel(R) Core(TM) i7-9700 CPU @ 3.00GHz 3.00 GHz GPU NVIDIA GeForce RTX 2080 Ti: Memory: 16 G System: Windows 10 (×64) Programming language: python 3.7		

The presented results demonstrate that deep learning-based approaches outperform traditional mathematical and statistical models, as well as machine learning methods, in predicting ground settlement. This improved accuracy is attributed to their ability to effectively leverage the nonlinear features present in time-series data. However, these models possess higher model complexity and require longer optimization and adjustment times for model parameters [62,63]. Additionally, due to its high time cost for constructing the model at each point in time, the ARIMA model is not recommended for large-scale subsidence prediction [64]. Evaluation of RNN, LSTM, and AT-LSTM models revealed that LSTM outperforms RNN in predicting time-series data [65]. The attention-based AT-LSTM model further improves on LSTM by accounting for temporal dependence in the ground settlement time-series data, leading to a higher accuracy of predictions. Our findings highlight the significance of temporal dependence in the model's prediction accuracy. Overall, the AT-LSTM model displays a superior performance and accuracy when compared to other evaluated algorithms.

4.4. Strengths and Limitations

The innovation of this paper is to propose and construct a ground subsidence prediction model AT-LSTM based on the attention mechanism and LSTM using the ground subsidence time-series data obtained from SBAS-InSAR processing. Using the Pingshuo mine as the study area for validation, the study shows that the model performed well in solving the large-scale ground subsidence prediction problem in mining areas, and the results have some reliability.

However, our study has certain limitations that need to be further discussed in the next study. From the spatial distribution of errors in the prediction results (Figure 17), it is evident that the model errors are spatially aggregated and have a certain relationship

with the form of coal mining. Subsequent studies need to consider the problem of spatial attribute, enhance the stability of the model in the mining area, and better provide services for the prediction of ground subsidence in the mining area.

5. Conclusions

In this study, the ground subsidence monitoring results for the period 2019–2022 in the Pingshuo mining area were obtained using the SBAS-InSAR technique with Sentinel-1A as the data source. Spatiotemporal processes were analyzed based on these results. Subsequently, a prediction method, named AT-LSTM, was proposed and constructed for the prediction of large-scale ground subsidence, based on the attention mechanism and LSTM. The research findings indicate that:

(1) Ground subsidence is serious in the Pingshuo mine area, with a vertical subsidence rate of −205.89–59.70 mm/yr for 2019–2022. Subsidence is concentrated in the JG-1 mine and the three open-pit areas of ATB, AJL, and DLT. The subsidence in the subsidence basin of the JG-1 mine area has increased the fastest, with the cumulative subsidence having reached 139 mm in December 2019, and the extent of subsidence has grown along the direction of the working from east to west. The three open-pit areas have seen a slower increase in subsidence than the JG-1 mine, with a continuous development trend in the extent of subsidence, consistent with the direction of open-pit stripping.

(2) The ground subsidence prediction results of the AT-LSTM model exhibit a spatial distribution that closely matches the actual situation, with prediction errors concentrated at ±2.0 mm. Compared with LSTM, the proposed model allows for better capturing of the time-varying characteristics of the data. Overall, the developed prediction method in this study demonstrates favorable performance and certain reliability for forecasting ground subsidence time-series data in mining areas.

(3) This paper presents an approach using SBAS-InSAR results to predict ground subsidence in mining areas, which alleviates the difficulty of data acquisition. By comparison with typical time-series prediction methods, the proposed approach in this study exhibits certain validity and feasibility, and can provide services for environmental management in mining areas.

In conclusion, this paper validates the feasibility of the AT-LSTM model based on time-series InSAR data for ground subsidence prediction in mining areas. Future work will focus on enhancing the robustness and accuracy of the prediction model through thorough consideration of the effects of mining processes and spatial location.

Author Contributions: Conceptualization, Y.L. and J.Z.; methodology, Y.L.; validation, Y.L.; formal analysis, Y.L.; software, Y.L.; investigation, Y.L.; resources, Y.L.; data curation, Y.L.; writing—original draft preparation, Y.L.; writing—review and editing, Y.L. and J.Z.; visualization, Y.L.; supervision, J.Z. All authors have read and agreed to the published version of the manuscript.

Funding: This research was funded by the Natural Science Foundation of China (No.42171424).

Data Availability Statement: The data used to support the findings of this study are available from the corresponding author upon request.

Acknowledgments: We thank all reviewers for their constructive comments on the manuscript.

Conflicts of Interest: The authors declare no conflict of interest.

References

1. York, R.; Bell, S.E. Energy Transitions or Additions?: Why a Transition from Fossil Fuels Requires More than the Growth of Renewable Energy. *Energy Res. Soc. Sci.* **2019**, *51*, 40–43. [CrossRef]
2. Ghadimi, P.; Wang, C.; Azadnia, A.H.; Lim, M.K.; Sutherland, J.W. Life Cycle-Based Environmental Performance Indicator for the Coal-to-Energy Supply Chain: A Chinese Case Application. *Resour. Conserv. Recycl.* **2019**, *147*, 28–38. [CrossRef]
3. Wang, G.; Xu, Y.; Ren, H. Intelligent and Ecological Coal Mining as Well as Clean Utilization Technology in China: Review and Prospects. *Int. J. Min. Sci. Technol.* **2019**, *29*, 161–169. [CrossRef]

4. Qian, L.; Wenzhong, Z.; Dai, W. Current Status, Challenges and Policy Recommendations Regarding the Sustainable Development of Mining Areas in China. *J. Resour. Ecol.* **2014**, *5*, 42–52. [CrossRef]
5. Zhu, D.; Chen, T.; Zhen, N.; Niu, R. Monitoring the Effects of Open-Pit Mining on the Eco-Environment Using a Moving Window-Based Remote Sensing Ecological Index. *Environ. Sci. Pollut. Res.* **2020**, *27*, 15716–15728. [CrossRef]
6. Hou, H.; Ding, Z.; Zhang, S.; Guo, S.; Yang, Y.; Chen, Z.; Mi, J.; Wang, X. Spatial Estimate of Ecological and Environmental Damage in an Underground Coal Mining Area on the Loess Plateau: Implications for Planning Restoration Interventions. *J. Clean. Prod.* **2021**, *287*, 125061. [CrossRef]
7. Loupasakis, C.; Angelitsa, V.; Rozos, D.; Spanou, N. Mining Geohazards—Land Subsidence Caused by the Dewatering of Opencast Coal Mines: The Case Study of the Amyntaio Coal Mine, Florina, Greece. *Nat. Hazards* **2014**, *70*, 675–691. [CrossRef]
8. Xue, Y.-Q.; Zhang, Y.; Ye, S.-J.; Wu, J.-C.; Li, Q.-F. Land Subsidence in China. *Environ. Geol.* **2005**, *48*, 713–720. [CrossRef]
9. Aobpaet, A.; Cuenca, M.C.; Hooper, A.; Trisirisatayawong, I. InSAR Time-Series Analysis of Land Subsidence in Bangkok, Thailand. *Int. J. Remote Sens.* **2013**, *34*, 2969–2982. [CrossRef]
10. Ferretti, A.; Prati, C.; Rocca, F. Permanent Scatterers in SAR Interferometry. *IEEE Trans. Geosci. Remote Sens.* **2001**, *39*, 8–20. [CrossRef]
11. Du, Z.; Ge, L.; Ng, A.H.-M.; Xiaojing, L.; Li, L. Mapping Land Subsidence over the Eastern Beijing City Using Satellite Radar Interferometry. *Int. J. Digit. Earth* **2018**, *11*, 504–519. [CrossRef]
12. Berardino, P.; Fornaro, G.; Lanari, R.; Sansosti, E. A New Algorithm for Surface Deformation Monitoring Based on Small Baseline Differential SAR Interferograms. *IEEE Trans. Geosci. Remote Sens.* **2002**, *40*, 2375–2383. [CrossRef]
13. Lanari, R.; Casu, F.; Manzo, M.; Zeni, G.; Berardino, P.; Manunta, M.; Pepe, A. An Overview of the Small BAseline Subset Algorithm: A DInSAR Technique for Surface Deformation Analysis. *Pure Appl. Geophys.* **2007**, *164*, 637–661. [CrossRef]
14. Li, S.; Xu, W.; Li, Z. Review of the SBAS InSAR Time-Series Algorithms, Applications, and Challenges. *Geod. Geodyn.* **2022**, *13*, 114–126. [CrossRef]
15. Dey, T.K.; Biswas, K.; Chakravarty, D.; Misra, A.; Samanta, B. Spatio-Temporal Subsidence Estimation of Jharia Coal Field, India Using SBAS-Dinsar with Cosmo-Skymed Data. In Proceedings of the IGARSS 2019—2019 IEEE International Geoscience and Remote Sensing Symposium, Yokohama, Japan, 28 July–2 August 2019; pp. 2123–2126.
16. Karamvasis, K.; Karathanassi, V. Performance Analysis of Open Source Time Series InSAR Methods for Deformation Monitoring over a Broader Mining Region. *Remote Sens.* **2020**, *12*, 1380. [CrossRef]
17. Chen, Y.; Tong, Y.; Tan, K. Coal Mining Deformation Monitoring Using SBAS-InSAR and Offset Tracking: A Case Study of Yu County, China. *IEEE J. Sel. Top. Appl. Earth Obs. Remote Sens.* **2020**, *13*, 6077–6087. [CrossRef]
18. Chen, Y.; Yu, S.; Tao, Q.; Liu, G.; Wang, L.; Wang, F. Accuracy Verification and Correction of D-InSAR and SBAS-InSAR in Monitoring Mining Surface Subsidence. *Remote Sens.* **2021**, *13*, 4365. [CrossRef]
19. Li, R.; Li, Z.; Han, J.; Lu, P.; Qiao, G.; Meng, X.; Hao, T.; Zhou, F. Monitoring Surface Deformation of Permafrost in Wudaoliang Region, Qinghai–Tibet Plateau with ENVISAT ASAR Data. *Int. J. Appl. Earth Obs. Geoinf.* **2021**, *104*, 102527. [CrossRef]
20. Liu, X.; Zhao, C.; Zhang, Q.; Yang, C.; Zhu, W. Heifangtai Loess Landslide Type and Failure Mode Analysis with Ascending and Descending Spot-Mode TerraSAR-X Datasets. *Landslides* **2020**, *17*, 205–215. [CrossRef]
21. Chen, D.; Lu, Y.; Jia, D. Land Deformation Associated with Exploitation of Groundwater in Changzhou City Measured by COSMO-SkyMed and Sentinel-1A SAR Data. *Open Geosci.* **2018**, *10*, 678–687. [CrossRef]
22. Wang, H.; Fu, H.; Zhu, J.; Liu, Z.; Zhang, B.; Wang, C.; Li, Z.; Hu, J.; Yu, Y. Estimation of Subcanopy Topography Based on Single-Baseline TanDEM-X InSAR Data. *J. Geod.* **2021**, *95*, 84. [CrossRef]
23. Li, B.; Wang, Z.; An, J.; Zhou, C.; Ma, Y. Time-Series Analysis of Subsidence in Nanning, China, Based on Sentinel-1A Data by the SBAS InSAR Method. *PFG—J. Photogramm. Remote Sens. Geoinf. Sci.* **2020**, *88*, 291–304. [CrossRef]
24. Chen, L.; Zhao, C.; Li, B.; He, K.; Ren, C.; Liu, X.; Liu, D. Deformation Monitoring and Failure Mode Research of Mining-Induced Jianshanying Landslide in Karst Mountain Area, China with ALOS/PALSAR-2 Images. *Landslides* **2021**, *18*, 2739–2750. [CrossRef]
25. Yuan, X.; Lin, M.; Han, B.; Zhao, L.; Wang, W.; Sun, J.; Wang, W. Observing Sea Surface Current by Gaofen-3 Satellite Along-Track Interferometric SAR Experimental Mode. *IEEE J. Sel. Top. Appl. Earth Obs. Remote Sens.* **2021**, *14*, 7762–7770. [CrossRef]
26. Potin, P.; Rosich, B.; Miranda, N.; Grimont, P.; Shurmer, I.; O'Connell, A.; Krassenburg, M.; Gratadour, J.-B. Copernicus Sentinel-1 Constellation Mission Operations Status. In Proceedings of the IGARSS 2019—2019 IEEE International Geoscience and Remote Sensing Symposium, Yokohama, Japan, 28 July–2 August 2019; pp. 5385–5388.
27. Giao, P.H.; Hue, V.T.; Han, N.D.; Anh, N.T.H.; Minh, N.N. Land Subsidence Prediction for a New Urban Mass Rapid Transit Line in Hanoi. *Undergr. Space* **2020**, *5*, 93–104. [CrossRef]
28. Li, Z.; Luo, Z.; Wang, Q.; Du, J.; Lu, W.; Ning, D. A Three-Dimensional Fluid-Solid Model, Coupling High-Rise Building Load and Groundwater Abstraction, for Prediction of Regional Land Subsidence. *Hydrogeol. J.* **2019**, *27*, 1515–1526. [CrossRef]
29. Cui, X.; Wang, J.; Liu, Y. Prediction of Progressive Surface Subsidence above Longwall Coal Mining Using a Time Function. *Int. J. Rock Mech. Min. Sci.* **2001**, *38*, 1057–1063. [CrossRef]
30. Zhang, G.; Xu, Z.; Chen, Z.; Wang, S.; Cui, H.; Zheng, Y. Predictable Condition Analysis and Prediction Method of SBAS-InSAR Coal Mining Subsidence. *IEEE Trans. Geosci. Remote Sens.* **2022**, *60*, 1–14. [CrossRef]
31. Rahmati, O.; Golkarian, A.; Biggs, T.; Keesstra, S.; Mohammadi, F.; Daliakopoulos, I.N. Land Subsidence Hazard Modeling: Machine Learning to Identify Predictors and the Role of Human Activities. *J. Environ. Manag.* **2019**, *236*, 466–480. [CrossRef]

32. Cieślik, K.; Milczarek, W. Application of Machine Learning in Forecasting the Impact of Mining Deformation: A Case Study of Underground Copper Mines in Poland. *Remote Sens.* **2022**, *14*, 4755. [CrossRef]
33. Zeng, C.-F.; Wang, S.; Xue, X.-L.; Zheng, G.; Mei, G.-X. Characteristics of Ground Settlement Due to Combined Actions of Groundwater Drawdown and Enclosure Wall Movement. *Acta Geotech.* **2022**, *17*, 4095–4112. [CrossRef]
34. Zeng, C.-F.; Chen, H.-B.; Liao, H.; Xue, X.-L.; Chen, Q.-N.; Diao, Y. Behaviours of Groundwater and Strata during Dewatering of Large-Scale Excavations with a Nearby Underground Barrier. *J. Hydrol.* **2023**, *620*, 129400. [CrossRef]
35. Ebel, B.A.; Loague, K.; Montgomery, D.R.; Dietrich, W.E. Physics-Based Continuous Simulation of Long-Term near-Surface Hydrologic Response for the Coos Bay Experimental Catchment: SIMULATION OF LONG-TERM HYDROLOGIC RESPONSE. *Water Resour. Res.* **2008**, *44*, W07417. [CrossRef]
36. Wang, Y.-Q.; Wang, Z.-F.; Cheng, W.-C. A Review on Land Subsidence Caused by Groundwater Withdrawal in Xi'an, China. *Bull. Eng. Geol. Environ.* **2019**, *78*, 2851–2863. [CrossRef]
37. Zhang, G.; Wu, Y.; Wang, L.; Zhang, K.; Daemen, J.J.K.; Liu, W. Time-Dependent Subsidence Prediction Model and Influence Factor Analysis for Underground Gas Storages in Bedded Salt Formations. *Eng. Geol.* **2015**, *187*, 156–169. [CrossRef]
38. Zhou, Q.; Hu, Q.; Ai, M.; Xiong, C.; Jin, H. An Improved GM(1,3) Model Combining Terrain Factors and Neural Network Error Correction for Urban Land Subsidence Prediction. *Geomat. Nat. Hazards Risk* **2020**, *11*, 212–229. [CrossRef]
39. Jiao, S.; Yu, J.; Simic Milas, A.; Li, X.; Liu, L. Assessing the Impact of Building Volume on Land Subsidence in the Central Business District of Beijing with SAR Tomography. *Can. J. Remote Sens.* **2017**, *43*, 177–193. [CrossRef]
40. Mohebbi Tafreshi, G.; Nakhaei, M.; Lak, R. A GIS-Based Comparative Study of Hybrid Fuzzy-Gene Expression Programming and Hybrid Fuzzy-Artificial Neural Network for Land Subsidence Susceptibility Modeling. *Stoch. Environ. Res. Risk Assess.* **2020**, *34*, 1059–1087. [CrossRef]
41. Wu, L.; Wang, J.; Zhou, J.; Yang, T.; Yan, X.; Zhao, Y.; Ye, Z.; Xu, N. Multi-Scale Geotechnical Features of Dredger Fills and Subsidence Risk Evaluation in Reclaimed Land Using BN. *Mar. Georesources Geotechnol.* **2020**, *38*, 947–969. [CrossRef]
42. Vaswani, A.; Shazeer, N.; Parmar, N.; Uszkoreit, J.; Jones, L.; Gomez, A.N.; Kaiser, L.; Polosukhin, I. Attention Is All You Need. *arXiv* **2017**, arXiv:1706.03762. [CrossRef]
43. Niu, Z.; Zhong, G.; Yu, H. A Review on the Attention Mechanism of Deep Learning. *Neurocomputing* **2021**, *452*, 48–62. [CrossRef]
44. Zhang, M.; Wang, J.; Li, S. Tempo-Spatial Changes and Main Anthropogenic Influence Factors of Vegetation Fractional Coverage in a Large-Scale Opencast Coal Mine Area from 1992 to 2015. *J. Clean. Prod.* **2019**, *232*, 940–952. [CrossRef]
45. Yang, W.; Sun, W.; Han, Q.; Li, S. Investigation on current situation of geological environment in Pinshuo coal mining area. *Coal Eng.* **2016**, *48*, 87–90.
46. Zhang, M.; Zhou, W.; Li, Y. The Analysis of Object-Based Change Detection in Mining Area: A Case Study with Pingshuo Coal Mine. *Int. Arch. Photogramm. Remote Sens. Spat. Inf. Sci.* **2017**, *XLII-2/W7*, 1017–1023. [CrossRef]
47. Zhou, W.; Yang, K.; Bai, Z.; Cheng, H.; Liu, F. The Development of Topsoil Properties under Different Reclaimed Land Uses in the Pingshuo Opencast Coalmine of Loess Plateau of China. *Ecol. Eng.* **2017**, *100*, 237–245. [CrossRef]
48. Bai, Z.; Yun, W. A case study on pingsshuo mining area: Land rehabilitation and reutilization in mining districts. *Resour. Ind.* **2008**, *10*, 32.
49. Wu, J.; Zhu, Q.; Qiao, N.; Wang, Z.; Sha, W.; Luo, K.; Wang, H.; Feng, Z. Ecological Risk Assessment of Coal Mine Area Based on "Source-Sink" Landscape Theory—A Case Study of Pingshuo Mining Area. *J. Clean. Prod.* **2021**, *295*, 126371. [CrossRef]
50. Liu, Y.; Qiu, H.; Yang, D.; Liu, Z.; Ma, S.; Pei, Y.; Zhang, J.; Tang, B. Deformation Responses of Landslides to Seasonal Rainfall Based on InSAR and Wavelet Analysis. *Landslides* **2022**, *19*, 199–210. [CrossRef]
51. Cohen, M.X. A Better Way to Define and Describe Morlet Wavelets for Time-Frequency Analysis. *NeuroImage* **2019**, *199*, 81–86. [CrossRef]
52. Fu, T. A Review on Time Series Data Mining. *Eng. Appl. Artif. Intell.* **2011**, *24*, 164–181. [CrossRef]
53. Esling, P.; Agon, C. Time-Series Data Mining. *ACM Comput. Surv.* **2012**, *45*, 1–34. [CrossRef]
54. Hochreiter, S.; Schmidhuber, J. Long Short-Term Memory. *Neural Comput.* **1997**, *9*, 1735–1780. [CrossRef]
55. Gers, F.A.; Schmidhuber, J.; Cummins, F. Learning to Forget: Continual Prediction with LSTM. *Neural Comput.* **2000**, *12*, 2451–2471. [CrossRef]
56. Kingma, D.P.; Ba, J. Adam: A Method for Stochastic Optimization. Available online: https://arxiv.org/abs/1412.6980v9 (accessed on 2 April 2023).
57. Liu, Q.; Zhou, W. Remote sensing monitoring and research on land subsidence in coal mining areas—A case study of Pingshuo mining area. In Proceedings of the 8th National Academic Conference on Land Reclamation and Ecological Restoration in Mining Areas, Henan, China, 12 October 2019; pp. 81–89.
58. Sun, J.; Zhang, J. Ground deformation monitoring of open-pit coal mine based on SBAS-InSAR and offset tracking techniques. *Saf. Coal Mines* **2022**, *53*, 162–169.
59. Zhao, H.; Ma, F.; Zhang, Y.; Guo, J. Monitoring and Analysis of the Mining-Induced Ground Movement in the Longshou Mine, China. *Rock Mech. Rock Eng.* **2013**, *46*, 207–211. [CrossRef]
60. Tang, W.; Motagh, M.; Zhan, W. Monitoring Active Open-Pit Mine Stability in the Rhenish Coalfields of Germany Using a Coherence-Based SBAS Method. *Int. J. Appl. Earth Obs. Geoinf.* **2020**, *93*, 102217. [CrossRef]
61. Liu, Q.; Zhang, Y.; Wei, J.; Wu, H.; Deng, M. HLSTM: Heterogeneous Long Short-Term Memory Network for Large-Scale InSAR Ground Subsidence Prediction. *IEEE J. Sel. Top. Appl. Earth Obs. Remote Sens.* **2021**, *14*, 8679–8688. [CrossRef]

62. Lim, B.; Zohren, S. Time-Series Forecasting with Deep Learning: A Survey. *Philos. Trans. R. Soc. A* **2021**, *379*, 20200209. [CrossRef]
63. Hewamalage, H.; Bergmeir, C.; Bandara, K. Recurrent Neural Networks for Time Series Forecasting: Current Status and Future Directions. *Int. J. Forecast.* **2021**, *37*, 388–427. [CrossRef]
64. Liu, Q.; Zhang, Y.; Deng, M.; Wu, H.; Kang, Y.; Wei, J. Time series prediction method of large-scale surface subsidence based on deep learning. *Acta Geod. Et Cartogr. Sin.* **2021**, *50*, 396–404.
65. Hua, Y.; Zhao, Z.; Li, R.; Chen, X.; Liu, Z.; Zhang, H. Deep Learning with Long Short-Term Memory for Time Series Prediction. *IEEE Commun. Mag.* **2019**, *57*, 114–119. [CrossRef]